Red perovskite LEDs by stabilising their octahedral structure

Lingmei Kong[1], Yuqi Sun[2], Bin Zhao[3], Kangyu Ji[2], Jie Feng[1], Jianchao Dong[3], Yuanzhi Wang[1], Zirui Liu[1], Shabnum Maqbool[2,4], Yunguo Li[5], Yingguo Yang[6,7], Linjie Dai[2], Wanhee Lee[8], Changsoon Cho[8,9], Samuel D. Stranks[2,4], Richard H. Friend[2], Ning Wang[3,]*, Neil C. Greenham[2,]*, Xuyong Yang[1,10]*

[1]Key Laboratory of Advanced Display and System Applications of Ministry of Education, Shanghai University, Shanghai, China.
[2]Cavendish Laboratory, University of Cambridge, Cambridge, UK.
[3]College of Physics, Jilin University, Changchun, China.
[4]Department of Chemical Engineering and Biotechnology, University of Cambridge, Cambridge, UK.
[5]CAS Key Laboratory of Crust-Mantle Materials and Environments, School of Earth and Space Sciences, University of Science and Technology of China, Hefei, China.
[6]Shanghai Synchrotron Radiation Facility (SSRF), Zhangjiang Lab, Shanghai Advanced Research Institute, Chinese Academy of Sciences, Shanghai, China.
[7]School of Microelectronics, Fudan University, Shanghai, China.
[8]Department of Material Science and Engineering, Pohang University of Science and Technology (POSTECH), Pohang, Republic of Korea.
[9]Institute for Convergence Research and Education in Advanced Technology, Yonsei University, Seoul, Republic of Korea.
[10]Shanghai Engineering Research Center for Integrated Circuits and Advanced Display Materials, Shanghai, China.

*Correspondence to: ningwang@jlu.edu.cn; ncg11@cam.ac.uk; yangxy@shu.edu.cn

Abstract

Light-emitting diodes based on metal halide perovskites (PeLEDs) with high colour quality and facile solution processing are promising candidates for full-colour and high-definition displays[1-4]. Despite the great success achieved in green PeLEDs with lead bromide perovskites[5], it is still challenging to realise pure-red (620-650 nm) LEDs using iodine-based counterparts, as they are constrained by the low intrinsic bandgap[6]. Here, we report efficient and colour-stable PeLEDs across the entire pure-red region, with a peak external quantum efficiency (EQE) reaching 28.7 per cent at 638 nm, enabled by incorporating a double-end anchored ligand molecule into pure-iodine perovskites. We demonstrate that a key function of the organic intercalating cation is to stabilise lead-iodine octahedron through coordination with exposed lead ions and enhanced hydrogen bonding with iodine, which synergistically facilitates spectral modulation, promotes charge transfer between perovskite quantum wells and reduces iodine migration under electrical bias. We realise continuously tunable emission wavelengths for iodine-based

perovskite films with suppressed energy loss caused by the decrease in bond energy of lead-iodine in ionic perovskites as the bandgap increases. Importantly, the resultant devices show outstanding spectral stability and half-lifetime of >7,600 minutes at an initial luminance of 100 cd m^{-2}.

Main text

Metal halide perovskites have gained tremendous attention for high-definition displays due to their high colour purity, tunable bandgap, together with facile solution processability[1-3]. Rapid progress has been made in the performance of PeLEDs[7-18], especially green ones with bromine (Br)-based perovskites, whose EQEs have approached 30%[5,19-21]. However, achieving efficient and colour-stable PeLEDs with pure-red emission (between 620 and 650 nm) — a prerequisite for one of the three primary colours in displays — remains a challenge[22,23]. The inherent bandgap of lead-bromide perovskite provides a natural advantage for achieving saturated green emission. In contrast, iodine (I)-based perovskites emit in the deep red (e.g., ~ 680 nm for $CsPbI_3$) or even the near-infrared region, originating from their narrow bandgap. Br-I mixing in perovskites is a widely used strategy to tune the bandgap towards pure-red emission region, but is susceptible to spectral shifting due to halide segregation under electrical bias[22]. Alternatively, reduced-dimensional I-based perovskites are strong competitors to mixed Br-I perovskites. Colloidal $CsPbI_3$ nanocrystals have been demonstrated to realise pure-red emission by the quantum size effect[24]. Nevertheless, in addition to the relatively complex synthesis, such colloidal nanocrystals suffer from insulating long-chain organic ligands that not only hinder carrier transport, but also contribute to instability as they are prone to detach from the soft lattice surface of perovskites[25,26].

Reduced-dimensional polycrystalline perovskite thin films with quantum well structure show facile film formation, highly efficient radiative recombination rates and potential for long-term stability in PeLEDs[27,28]. So far, spacer engineering for tailoring energy cascade channels has been extensively developed to realise pure-red emission[29]. Unfortunately, the EQE of PeLEDs based on Ruddlesden-Popper perovskite is only 12.4%[30], far behind the state of the art, and reduced-dimensional red PeLEDs that simultaneously exhibit high efficiency and spectral stability have not yet been demonstrated. More importantly, very few of the above solution-processed perovskites could achieve spectrally stable emission under photoexcitation, and is even rarer for high voltage biases. The lack of options for spectrally stable pure-red emission has the potential to limit the display applications of PeLED technology.

Octahedron stabilisation strategy

We sought to stabilise the I-Pb-I octahedron of black-phase in reduced-dimensional $CsPbI_3$ perovskites by using ammonium ligands with multiple binding sites as lattice stabilizer that could also simultaneously increase the perovskite bandgap for pure-red emission. The traditional ammonium ligands such as phenylethyl ammonium (PEA) bind to perovskite through weak hydrogen bonding that provides limited bonding force to anchor the lattice[19], while the introduction of excess long-chain ligands in turn sacrifices the electrical properties of perovskites. 3-Methoxyphenethyl-ammonium (MOPA, or methoxy-PEA) with ammonium at the head and a methoxy group at the tail is an ideal molecular configuration to anchor perovskites and concurrently increases the bandgap due to the large steric hindrance. The adsorption modes and corresponding formation energies of MOPA on the perovskite surface are investigated, including head, tail, and double-end types of connection (Fig. 1a). The larger averaged integrated crystal orbital Hamilton populations (ICOHP)[31] of the O-Pb (0.207 eV/interaction) and N-I (0.048 eV/interaction) bonds indicate higher binding forces than those of N-Pb and O-I (Supplementary Fig. 1 and Supplementary Table 1). Note that the formation energy of the tail connection mode shows a positive value, indicating that such a connection is almost impossible, mainly due to the steric hindrance of methyl group (Fig. 1b). By contrast, the models show a high probability for the formation of head or double-end connection, suggesting that both of them can exist on the perovskite surface. As has been widely reported[32,33], the head connection mode breaks the originally continuous three-dimensional $CsPbI_3$ structure and leads to reduced-dimensional perovskites.

To study the effect of double-end connected MOPA on the Ruddlesden-Popper (RP) structured perovskite, time-dependent bond angles of I-Pb-I in the top perovskite without and with MOPA anchoring are investigated. We observed that the bond angles of perovskite without MOPA are fluctuated in a large scale (approximately from 76° to 96°) (Fig. 1c). This implies that a lower electric field driving can cause I^- to leave the lattice site (Extended Data Fig. 1), which leads to iodide vacancies and local crystallographic disorder acting as non-radiative recombination defects, restricting both the luminous efficiency and stability. In contrast, bond angle in MOPA-perovskite can be stable in the range of 80°-92°. The corresponding standard deviation of bond angle is significantly reduced in MOPA-perovskite (Fig. 1d), indicating a more stable inorganic octahedral framework. Further, the similar trends have been confirmed by theoretical simulations with a Cs-I terminated model (Supplementary Fig. 2) and an extended structural model where MOPA ligands are sandwiched between the adjacent perovskite layers (Supplementary Fig. 3).

Pure red emission characteristics

We experimentally incorporated MOPA into $CsPbI_3$ perovskite in gradually increasing amounts to obtain reduced-dimensional perovskites with pure-red emission by continuously expanding the bandgap. We found that, when the molar ratio of MOPA/Pb in the precursor is less than 1, symmetric photoluminescence (PL) is observed and the corresponding PL centre is about 653 nm (Extended Data Fig. 2a). At higher molar ratios, a blue-shift is observed in the main peak, but it is accompanied by the appearance of a distinct high-energy peak which we attribute to the formation of multiple phases with inefficient energy transfer[34-36]. To optimise the energy cascade channels to achieve pure-red PL emission with enhanced luminous efficiency, we took advantage of the synergistic effect from another two ligands, *α*-methylbenzyl-ammonium (MBA) and 1-methyl-3-phenylpropyl-ammonium (MPPA), whose steric hindrances and electrical properties are obviously distinct (Inset in Fig. 1e). The resultant perovskite films with both MBA and MPPA (denoted as ‘M-MPPA’) exhibit efficient PL emission peaking at ~ 665 nm with no high-energy shoulder, as well as good film quality (Extended Data Fig. 2b-d and Supplementary Figs. 4, 5). As a result, continuously tunable PL wavelengths are obtained in the pure-red region from 650 nm to 620 nm by adding variable amounts of MOPA into M-MPPA based perovskites (denoted as ‘MM-MOPA’) (Fig. 1e, Extended data Fig. 2e and Supplementary Fig. 6). It is noteworthy that the MOPA-based perovskite exhibits longer PL lifetime compared to the perovskite with only MPPA or MBA at the same emission position, implying fewer non-radiative recombination sites (Extended Data Fig. 2f). Therefore, as the bandgap widens, MM-MOPA perovskite films show much higher photoluminescence quantum yields (PLQYs) compared to M-MPPA ones (Fig. 1f and Supplementary Fig. 7a). We argued that the improvement is due to the reduction of iodine-vacancy traps and exposed Pb^{2+}. X-ray photoelectron spectroscopy (XPS) measurements were carried out to examine the interaction between MOPA and perovskite. The MM-MOPA perovskite shows that the N 1*s* peak is shifted towards lower binding energy by ~0.2 eV, while this shift is not observed in M-MPPA perovskites (Fig. 1g and Supplementary Fig. 8a). This demonstrates that the electron cloud around N in the ammonium moiety is displaced due to a stronger hydrogen-bond interaction between N-H···I[37]. We attributed the stronger hydrogen-bond interaction to the reduced molecular disturbance of MOPA due to the coordination between O in MOPA and exposed Pb^{2+} on the octahedron[38]. This effect is also corroborated by the shift of C-O in Fourier transform infrared (FTIR) spectroscopy[39], Pb 4*f* and O 1*s* XPS spectra, and solid-state ^{207}Pb and ^{1}H nuclear magnetic resonance (NMR) signals of the MM-MOPA perovskites (Extended Data Fig. 3 and Supplementary Fig. 8b).

Effects of MOPA on perovskites

We then studied the effect of the MOPA ligand on the crystallization kinetics of perovskites by using in situ PL measurements combined with synchrotron-based in situ grazing-incidence wide-angle X-ray scattering (GIWAXS). The evolution of PL spectra of M-MPPA and MM-MOPA perovskite films with increasing annealing time is shown in Fig. 2a. We observed that the emission peaks for both the samples are red-shifted during the initial ~160 s due to increase of the size and hence decrease of quantum confinement effect, but the MM-MOPA perovskite shows a smaller PL shift than the M-MPPA one (Supplementary Fig. 9), suggesting that the strong interaction between perovskite and MOPA leads to a smaller nuclei size and slower nucleation kinetics of perovskite[40]. This facilitates the formation of these low-dimensional species in MM-MOPA perovskite that correspond to pure red emission. As shown in Fig. 2b and Extended Data Fig. 4, in situ GIWAXS pattern signals from $n = 2$ and 3 species (n, the number of perovskite octahedron layers) were observed throughout the film formation process, which are also revealed by X-ray diffraction (XRD) patterns and transient absorption spectra (Supplementary Figs. 10, 11). From temperature-dependent PL analysis (Extended Data Fig. 5), we observed a higher exciton binding energy (E_b = 209 ± 20 meV) in MM-MOPA perovskite than that of M-MPPA (160 ± 13 meV) due to the strengthened confinement effect through MOPA anchoring[5]. The PL shift and the gradually weakened intensity as temperature increases are also suppressed in MM-MOPA perovskite, indicating that the thermally activated nonradiative recombination process is inhibited[41]. We further checked the crystal quality of MM-MOPA perovskite films since bulk/surface defects can act as a cause of ion migration and carrier trapping, thereby significantly impairing the luminous efficiency and material stability[5,42]. The MM-MOPA perovskite film exhibits obviously increased PL lifetime compared to M-MPPA perovskite (τ = 25.5 ns *versus* 3.4 ns, Fig. 2c and Supplementary Fig. 7), suggesting a decrease in defect density for MM-MOPA perovskite. Space charge-limited current (SCLC) measurements reveal a trap density (n_t) of 2.6×10^{16} cm^{-3} for MM-MOPA perovskite, which is approximately half that in M-MPPA (4.1×10^{16} cm^{-3}) (Fig. 2d, e). We tested the PL stability of MM-MOPA perovskite films by using time-dependent normalized PL measurements. In contrast to the sharp reduction of PL intensity in the perovskite without MOPA, we observed that both the structural stability and photostability are dramatically improved for the MM-MOPA perovskite films (Extended Data Fig. 6).

We characterised the electrical properties for the perovskite films. The mobility of MM-MOPA perovskite film is 2-fold higher than that of M-MPPA sample (3.7 ± 0.3 cm^2 V^{-1} s^{-1} versus 1.8 ± 0.2 cm^2 V^{-1} s^{-1}). Also, a higher surface potential in MM-MOPA perovskite revealed by Kelvin probe force microscopy (KPFM) contact potential difference images implies the better charge transport[43] (Supplementary Fig. 12). A Bader analysis shows a notably improved atom charge on C atoms of the adjacent MPPA upon adding MOPA (Supplementary Fig. 13). This suggests that the O in MOPA facilitates the charge transfer across the van der Waals' gap of the adjacent individual perovskite layers. The distribution of electrostatic potentials between MPPA and MOPA molecules further confirms that this charge transfer arises from the electron-withdrawing property of the methoxy group (Supplementary Fig. 14). The conductivity (σ) of MM-MOPA perovskite film also shows 3-fold higher than that of M-MPPA perovskite due to the increased mobility (Fig. 2f).

Light-emitting diode performance

Encouraged by the promising results from film characterisation, PeLEDs based on the MM-MOPA perovskite films are fabricated with an architecture depicted in Fig. 3a and Supplementary Fig. 15. Matched energy level alignment between carrier transport layers and perovskite is obtained to minimise operating voltage (Supplementary Fig. 16). The champion PeLEDs show electroluminescence (EL) spectra centred at 638 nm with Commission Internationale de l'Eclairage (CIE) coordinates (0.69, 0.31), and retain a constant emission wavelength under different voltages (Fig. 3b). The angle-dependent EL intensity is in accord with a Lambertian profile (Fig. 3c). The EQE of the LED reaches a maximum of 28.7% at a current density of 0.22 mA cm^{-2} (Fig. 3d, e), which is close to the theoretical efficiency value and is considerably higher than that of the M-MPPA based PeLEDs (a peak EQE of 16.4%) (Supplementary Fig. 17 and Supplementary Table 2). Optical simulations revealed that the outcoupling factor of the PeLED is up to ~29.7% and photon-recycling contributes 10.4% of the overall emission (Supplementary Figs. 18 and 19). An EQE of 27.9% is also certified at National Institute of Measurement and Testing Technology (Supplementary Fig. 20), comparable to that measured in the lab. The inset in Fig. 3e displays a bright and uniform pure-red emission over an active area of 30 mm × 30 mm, suggesting the potential for high-quality large-area LEDs.

The general applicability of this approach to improving the stability and efficiency of I-based perovskite devices is demonstrated by fabricating pure-red PeLEDs emitting at different wavelengths. The highest EQEs reach 22.2% at 627 nm and 28.7% at 645 nm, respectively (Extended Data Fig. 7). The statistical data show high average EQEs of 20.2 ± 1.8% at 627 nm, 26.6 ± 1.6% at 638 nm and 25.1 ± 2.2% at 645 nm (Fig. 3f), indicating excellent reproducibility from device to device. To our knowledge, the device efficiency values achieved in this work surpass all the reported I-based and even Br-I mixed pure-red PeLEDs at the respective emission wavelengths (Fig. 3g, Supplementary Fig. 21 and Extended Data Table 1). The devices with different emission wavelengths also present good operational stability and spectral stability (Fig. 3h, Extended Data Fig. 8 and Supplementary Figs. 22-24). Specifically, our target PeLED demonstrated a half-lifetime of 7,610 min at an initial luminance of 100 cd m^{-2}, approximately 12-fold longer than the best reported efficient pure-red PeLEDs, and there is almost no spectral change observed before and after the device lifetime measurements.

The EL intensity uniformity and spectral stability of devices are further investigated by hyperspectral microscopy. When the applied voltage increases from 6 to 8 V, in addition to a significant decrease in uniformity of EL intensity, the EL peak wavelength becomes spatially inhomogeneous in M-MPPA based PeLED (Fig. 4a and Extended Data Fig. 9a-c). The migration of I^- under high field causes local crystallographic and energy structural disorder that not only provides non-radiative recombination centres but also leads to spectral drift[7], which are mitigated by MOPA. Consequently, MM-MOPA based PeLEDs show more spatially uniform EL emission at a high voltage of 8 V (Fig. 4b and Extended Data Fig. 9d-f). We performed transient EL measurements, where the devices were driven by 6V/0V (on/off) voltage pulses with a duration of 500 ns at a frequency of 1 MHz. Time-resolved EL spectra were measured by an iCCD system in a 10 ns window after a delay that was varied from 0 to 2,000 ns in 10 ns steps following device turn-on, tracking the EL kinetics over two pulses. The total experimental measurement time for each device was approximately 6 min. As shown in Fig. 4c and d, both devices exhibit similar EL kinetics between 0 and 1,000 ns. As the devices suffered from degradation under intense voltage pulses during the course of the experiment, the peak EL intensities of both devices measured for time delays between 1,000 and 2,000 ns dropped. The peak EL intensity of M-MPPA device between 1,000 to 2,000 ns drops to 65% of its peak value between 0 to 1,000 ns (Supplementary Fig. 25). However, MM-MOPA device shows mitigated device degradation and retains 80% of its first peak EL intensity, consistent with other measurements. We noticed a delay in the EL onset time of the M-MPPA device in the period from 1,000 to 2,000 ns, compared to the MM-MOPA device. If we assume the

RC time constant of the devices remains unchanged, this delay in the EL onset is associated with slower carrier transport within the device due to device degradation[44]. However, no such increase in EL onset time was detected in the MM-MOPA device, implying its improved stability. To visually monitor the cause of failure at the device level, we conducted time-of-flight secondary ion mass spectrometry (ToF-SIMS) depth profiling for devices before and after aging. From ToF-SIMS results (Fig. 4e, f and Supplementary Fig. 26), in full agreement with our theoretical and spectroscopic analysis, the I^- ions are severely accumulated at the indium tin oxide (ITO) anode driven by electric field in the M-MPPA based PeLEDs, which is one of the main factors causing the fast device failure. With the MOPA anchoring perovskite octahedron, the I^- migration is effectively inhibited, leading to significantly improved device stability.

In this work, a double-end anchored ligand molecule with ammonium and methoxy groups, MOPA, is incorporated into reduced-dimensional perovskite to stabilise the inorganic framework by strengthening hydrogen bonding interaction and coordinating lead ions, resulting in the suppression of I^- migration under electric field and reduction of non-radiative recombination. MOPA also induces strong quantum confinement to enlarge the perovskite bandgap and facilitates charge transfer across the van der Waals' gap due to the electron-withdrawing nature of the methoxy group. These improvements allow us to achieve EQEs over 20% in the entire pure-red region (EQE of the champion PeLED reaches 28.7%), stable and uniform EL emission and significantly improved operational lifetime. Our results demonstrate a highly promising route for PeLEDs towards full-colour display with high colour purity and this fundamental advance could also be applicable to halide perovskite semiconductors of various colours, paving the way for reaching Rec. 2020 standard.

References

1 Tan, Z.-K. et al. Bright light-emitting diodes based on organometal halide perovskite. *Nat. Nanotechnol.* **9**, 687-692 (2014).

2 Kim, Y. H. et al. Multicolored organic/inorganic hybrid perovskite light-emitting diodes. *Adv. Mater.* **27**, 1248-1254 (2015).

3 Cho, H. et al. Overcoming the electroluminescence efficiency limitations of perovskite light-emitting diodes. *Science* **350**, 1222-1225 (2015).

4 Wang, N. et al. Perovskite light-emitting diodes based on solution-processed self-organized multiple quantum wells. *Nat. Photonics* **10**, 699-704 (2016).

5 Kim, J. S. et al. Ultra-bright, efficient and stable perovskite light-emitting diodes. *Nature* **611**, 688-694 (2022).

6 Hassan, Y. et al. Ligand-engineered bandgap stability in mixed-halide perovskite LEDs. *Nature* **591**, 72-77 (2021).

7 Sun, Y. et al. Bright and stable perovskite light-emitting diodes in the near-infrared range. *Nature* **615**, 830-835 (2023).

8 Jiang, Y. et al. Synthesis-on-substrate of quantum dot solids. *Nature* **612**, 679-684 (2022).

9 Cao, Y. et al. Perovskite light-emitting diodes based on spontaneously formed submicrometre-scale structures. *Nature* **562**, 249-253 (2018).

10 Dong, Y. et al. Bipolar-shell resurfacing for blue LEDs based on strongly confined perovskite quantum dots. *Nature Nanotechnol.* **15**, 668-674 (2020).

11 Guo, B. et al. Ultrastable near-infrared perovskite light-emitting diodes. *Nat. Photonics* **16**, 637-643 (2022).

12 Zhao, B. et al. High-efficiency perovskite-polymer bulk heterostructure light-emitting diodes. *Nat. Photonics* **12**, 783-789 (2018).

13 Xu, W. et al. Rational molecular passivation for high-performance perovskite light-emitting diodes. *Nat. Photonics* **13**, 418-424 (2019).

14 Liu, Y. et al. Bright and stable light-emitting diodes based on perovskite quantum dots in perovskite matrix. *J. Am. Chem. Soc.* **143**, 15606-15615 (2021).

15 Liu, Y. et al. Efficient blue light-emitting diodes based on quantum-confined bromide perovskite nanostructures. *Nat. Photonics* **13**, 760-764 (2019).

16 Kim, Y.-H. et al. Comprehensive defect suppression in perovskite nanocrystals for high-efficiency light-emitting diodes. *Nat. Photonics* **15**, 148-155 (2021).

17 Kuang, C. et al. Critical role of additive-induced molecular interaction on the operational stability of perovskite light-emitting diodes. *Joule* **5**, 618-630 (2021).

18 Liu, M. et al. Suppression of temperature quenching in perovskite nanocrystals for efficient and thermally stable light-emitting diodes. *Nat. Photonics* **15**, 379-385 (2021).

19 Ma, D. et al. Distribution control enables efficient reduced-dimensional perovskite LEDs. *Nature* **599**, 594-598 (2021).

20 Lin, K. et al. Perovskite Light-emitting diodes with external quantum efficiency exceeding 20 per cent. *Nature* **562**, 245-248 (2018).

21 Liu, Z. et al. Perovskite light-emitting diodes with EQE exceeding 28% through a synergetic dual-additive strategy for defect passivation and nanostructure regulation. *Adv. Mater.* **33**, 2103268 (2021).

22 Vashishtha, P. & Halpert, J. E. Field-driven ion migration and color instability in red-emitting mixed halide perovskite nanocrystal light-emitting diodes. *Chem. Mater.* **29**, 5965-5973 (2017).

23 Han, T.-H. et al. A roadmap for the commercialization of perovskite light emitters. *Nat. Rev. Mater.* **7**, 757-777 (2022).

24 Protesescu, L. et al. Nanocrystals of cesium lead halide perovskites ($CsPbX_3$, X = Cl, Br, and I): novel optoelectronic materials showing bright emission with wide color gamut. *Nano Lett.* **15**, 3692-3696 (2015).

25 Li, J. et al. 50-fold EQE improvement up to 6.27% of solution-processed all-inorganic perovskite $CsPbBr_3$ QLEDs via surface ligand density control. *Adv. Mater.* **29**, 1603885 (2017).

26 Huang, H., Bodnarchuk, M. I., Kershaw, S. V., Kovalenko, M. V. & Rogach, A. L. Lead halide perovskite nanocrystals in the research spotlight: stability and defect tolerance. *ACS Energy Lett.* **2**, 2071-2083 (2017).

27 Yuan, M. et al. Perovskite energy funnels for efficient light-emitting diodes. *Nat.*

Nanotechnol. **11**, 872-877 (2016).

28 Lin, Y. et al. Suppressed ion migration in low-dimensional perovskites. *ACS Energy Lett.* **2**, 1571-1572 (2017).

29 Qing, J. et al. Spacer cation alloying in ruddlesden-popper perovskites for efficient red light-emitting diodes with precisely tunable wavelengths. *Adv. Mater.* **33**, 2104381 (2021).

30 Yang, L. et al. Pure red light-emitting diodes based on quantum confined quasi-two-dimensional perovskites with cospacer cations. *ACS Energy Lett.* **6**, 2386-2394 (2021).

31 Nelson, R. et al. LOBSTER: Local orbital projections, atomic charges, and chemical-bonding analysis from projector-augmented-wave-based density-functional theory. *J. Comput. Chem.* **41**, 1931-1940 (2020).

32 Xiao, Z. et al. Efficient perovskite light-emitting diodes featuring nanometre-sized crystallites. *Nat. Photonics* **11**, 108-115 (2017).

33 Shang, Y. et al. Highly stable hybrid perovskite light-emitting diodes based on Dion-Jacobson structure. *Sci. Adv.* **5**, eaaw8072 (2019).

34 Tian, Y. et al. Highly efficient spectrally stable red perovskite light-emitting diodes. *Adv. Mater.* **30**, 1707093 (2018).

35 Wang, K. et al. Suppressing phase disproportionation in quasi-2D perovskite light-emitting diodes. *Nat. Commun.* **14**, 397 (2023).

36 Tremblay, M.-H. et al. Hybrid organic lead iodides: role of organic cation structure in obtaining 1D chains of face-sharing octahedra vs 2D perovskites. *Chem. Mater.* **34**, 935-946 (2022).

37 Aakeröy, C. B. & Seddon, K. R. The hydrogen bond and crystal engineering. *Chem. Soc. Rev.* **22**, 397-407 (1993).

38 Liao, Y. et al. Anti-dissociation passivation via bidentate anchoring for efficient carbon-based $CsPbI_{2.6}Br_{0.4}$ solar cells. *Adv. Funct. Mater.* **33**, 2214784 (2023).

39 Sun, X. et al. Methoxy functionalization of phenethylammonium ligand for efficient perovskite light-emitting diodes. *Adv. Opt. Mater.* **11**, 2300464 (2023).

40 Shi, P. et al. Oriented nucleation in formamidinium perovskite for photovoltaics. *Nature* **620**, 323-327 (2023).

41 Han, D. et al. Tautomeric mixture coordination enables efficient lead-free perovskite LEDs. *Nature* **622**, 493-498 (2023).

42 Saidaminov, M. I. et al. Suppression of atomic vacancies via incorporation of isovalent small ions to increase the stability of halide perovskite solar cells in ambient air. *Nat. Energy* **3**, 648-654 (2018).

43 Wang, R. et al. Constructive molecular configurations for surface-defect passivation of perovskite photovoltaics. *Science* **366**, 1509-1513 (2019).

44 Xu, M. et al. A transient-electroluminescence study on perovskite light-emitting diodes. *Appl. Phys. Lett.* **115**, 041102 (2019).

Figure Captions

Fig. 1 | Interaction and configuration between MOPA and perovskite. a,**b**, Adsorption models (**a**) and their corresponding formation energies (**b**) of MOPA ligand on the perovskite surface via head, tail, and double-end connections simulated with Pb-I terminated model. **c**,**d**, Time-dependent bond angles (**c**) and the corresponding standard deviation (**d**) of I-Pb-I in $CsPbI_3$ without (W/O) and with MOPA. **e**, PL spectra of MM-MOPA perovskite films. Inset shows the chemical structures of MBA, MPPA and MOPA, respectively. **f**, PLQYs for the perovskite films with various bandgaps. **g**, N 1*s* spectra of perovskite films.

Fig. 2 | Optoelectronic characterisations. a, In situ PL characterisation of perovskite films. The evolution of PL peak with annealing time is marked by arrows. **b**, In situ GIWAXS characterisation of the MM-MOPA perovskite film. **c**, Time-resolved PL spectra of perovskite films. **d**,**e**, SCLC measurements of hole-only devices based on M-MPPA (**d**) and MM-MOPA (**e**). **f**, Conductivity measurements for the perovskite films.

Fig. 3 | Device performance of the pure-red PeLEDs. a, Device structure of PeLEDs. **b**, EL spectra of a PeLED under different driving voltages. Inset shows the corresponding CIE chromatic coordinates (0.69, 0.31). **c**, An angle-dependent EL of PeLEDs. **d**,**e**, *J*-*V*-*L* (**d**) and corresponding EQE-*J* (**e**) curves of the PeLEDs based on MM-MOPA perovskite. Inset in e, an optical photo of PeLED operated under a bias voltage of 4 V with an active area of 900 mm^2. **f**, EQE statistics of PeLEDs at different EL wavelengths (10 devices each). **g**, Summary of the reported peak EQEs of red PeLEDs (620-650 nm) based on pure-I compositions (Extended Data Table 1). **h**, Half-lifetime measurements for MM-MOPA based PeLEDs emitting at 645 nm.

Fig. 4 | Stability analysis of PeLEDs. a,**b**, Hyperspectral EL images of PeLEDs based on M-MPPA (**a**) and MM-MOPA (**b**) at an operating voltage of 8 V. Scale bar, 10 μm. **c**,**d**, EL kinetics of PeLEDs based on M-MPPA (**c**) and MM-MOPA (**d**) under the same voltage pulse of 6 V. **e**,**f**, ToF-SIMS depth profiling conducted on the PeLEDs based on M-MPPA (**e**) and MM-MOPA (**f**) before and after being driven. HTL, hole transport layer.

Methods

Materials

Lead iodide (PbI_2, 99.999%), cesium iodide (CsI, 99.999%), α-methylbenzylamine (also known as 1-phenylethylamine), polyvinylpyrrolidone (PVP), and N,N-dimethylformamide (DMF, 99.8%) were purchased from Sigma-Aldrich. 3-Methoxyphenethylamine and 1-methyl-3-phenylpropylamine were purchased from Aladdin. 2′,2′-(1,3,5-Benzinetriyl)-tris(1-phenyl-1-H-benzimidazole)) (TPBi) and lithium fluoride (LiF) were purchased from Luminescence Technology Corp. Poly(ethylenedioxythiophene):polystyrenesulfonate (PEDOT:PSS, Heraeus-Clevios P VP AI4083) and poly[bis(4-phenyl)(2,4,6-trimethylphenyl)amine] (PTAA) were purchased from Xian Yuri Solar Co, Ltd. All chemicals were used as received without further purification.

Synthesis of ammonium salt

MBAI, MPPAI and MOPAI were respectively synthesized by adding hydroiodic acid into a solution of α-methylbenzylamine, 1-methyl-3-phenylpropylamine and 3-methoxyphenethylamine in anhydrous ethanol with stirring continuously for 6 h in an ice bath. The precipitate was obtained by evaporating the solution at 60 °C, washed using diethyl ether for three times and then dried under vacuum.

Perovskite precursor solutions

For basic perovskite precursors, PbI_2, CsI, MBAI, and MPPAI were dissolved in DMF with the ratio of 1:0.75:0.5:0.5, in which the molar concentration of Pb^{2+} is 0.12 M. For the MM-MOPA/M-MPPA perovskites, MOPAI/MPPAI was further added into the basic precursor solutions at a concentration range of 0.01 - 0.05 M. The mixture was stirred at 60 °C overnight and filtered through a 0.45 μm polytetrafluoroethylene membrane before use.

Device fabrication

PEDOT:PSS layer was spin-coated onto the oxygen-plasma-treated ITO substrate at 4,000 r.p.m. for 40 s, and then baked at 150 °C for 20 min in ambient air. Subsequently, the ITO substrate was transferred into a nitrogen-filled glovebox. PTAA (8 mg mL^{-1} in chlorobenzene) was spin-coated on the PEDOT:PSS at 4,000 r.p.m. for 40 s, followed by annealing at 120 °C for 20 min. PVP (3 mg mL^{-1} in absolute ethyl alcohol) was then spin-coated on PTAA film. Perovskite was spin-coated at 4,500 r.p.m. for 40 s and basked at 80 °C for 5-8 min. After that, TPBi (40-50 nm), LiF (1 nm), and Al electrode (100 nm) were thermally evaporated with vacuum pressure below 4×10^{-4} Pa, respectively.

PeLED characterisations

The used device active area was 4 mm^2, and the electroluminescence performance were tested by using a Keithley 2400 source meter, a Shenzhen Pynect integrating sphere (50 mm in diameter) and a QE Pro spectrometer (Ocean Optics) in a nitrogen-filled glovebox at room temperature. Angular dependence of emission intensity was collected using a Konica Minolta CS-200 detector. The device characteristics were cross-checked by a system comprising a PR-670 spectroradiometer (Photo Research) coupled with a Keithley 2400 source meter unit. The operational lifetime of encapsulated PeLEDs were performed using a commercialized ZJZCL-1 OLED ageing lifespan test system in a nitrogen-filled glovebox. For transient EL measurements, the devices were electrically triggered by a functional generator (HP8116A, rise time < 7 ns) using 6 V square voltage pulses with a width of 500 ns for the on cycles (forward bias) at a repetition rate of 1 MHz. The off cycles were 0 V (zero bias). Time-resolved EL spectra of the devices were measured by an intensified CCD (iCCD) system (Andor iStar DH740) connected to a calibrated grating spectrometer (Andor SR303i). The EL output was measured in a 10 ns window delayed from the voltage turn on by a time that was varied between 0 and 2000 ns in 10 ns steps.

Perovskite film characterisations

XPS and UPS spectra were measured by Thermo scientific NexsaG2. A monochromatic Al Kα line (1486.6 eV) was used for XPS, and He I radiation (21.2 eV) was used for UPS. XRD patterns were collected on a Bruker D8 Advance diffractometer with Cu Kα radiation as X-ray source, ranging from 5° to 50° at a scanning rate of 3° min^{-1}. UV-Vis spectra were recorded on a Perkin Elmer Lambda 950 UV-Vis-NIR spectrometer. FTIR measurements were performed by using a Fourier-transform spectrometer (Nicolet 6700). Perovskite powder and MOPAI powder samples were prepared by a potassium bromide tabletting method with background subtraction. KPFM contact potential difference measurements were obtained using a Digital Instruments Multimode AFM (Veeco Metrology Group). Morphology of the perovskite films was characterized by scanning electron microscopy (FEI Magellan 400, USA) and atomic force microscopy (NTEGRA, NTMDT). In situ PL spectra were collected by using a QE Pro spectrometer. The PL stability test was performed with 365 nm UV light under a power of 4 W. Steady-state PL spectra and absolute PLQYs were measured using Edinburgh Instruments FS5 spectrofluorometer (Livingston, UK) comprising a mountable integrating sphere and a 150 W xenon lamp, while the time-resolved PL measurements were carried out in the same instrument using a nanosecond flash lamp as an excitation source (λ_{ex} = 365 nm). Power-density-dependent time-resolved PL spectra were measured using a 405 nm laser. The excitation-intensity-dependent PLQYs were performed using a homemade instrument combined a 405 nm laser, spectrometer, and optical integrating sphere. For temperature-dependent PL measurements, a cryostat (Janis ST-100) and liquid nitrogen were used and the perovskite films were excited by a continuous wave laser at an λ_{ex} of 400 nm (power density of 2 µJ cm^{-2}). Hall mobilities of perovskite films were measured by a Hall effect measurement system (Ecopia, HMS-7000) equipped with a calibrated blue LED (λ = 465 nm, max. power: 20 W) under a high signal-to-noise ratio[45,46]. Perovskite films solution-grown on fused silica substrate were deposited with 4-probe Au contacts in a desired Hall bar geometry. Photoexcitation was generated by illumination of blue LED. Conductivity of film was measured by semiconductor parameter analyzer (Keithley, 4200) with a probe station (LakeShore, TTP4). For details, 100 nm Ag was deposited on glass/perovskite film by thermal evaporation to form the anode and cathode electrodes through a shadow-mask with the channel width of 1,000 µm and channel length of 50 µm.

NMR measurement

Solid-state ^{1}H NMR experiments were performed on a Bruker Avance III 600 MHz NMR spectrometer equipped with a 3.2 mm magic-angle spinning (MAS) probe. The spectra were recorded using a single-pulse excitation pulse sequence, the spinning rate was set to 20 kHz, and the recycle delay was 2 s. All ^{1}H chemical shifts were calibrated using adamantane (δ = 19.1 ppm). Solid-state ^{207}Pb NMR spectra were acquired using a Bruker Avance III 300 MHz NMR spectrometer equipped with a two-channel static polarization enhancement (PE) probe, which were recorded using a single-pulse excitation pulse sequence with a recycle delay of 1 s. ^{207}Pb NMR spectra were referenced to $PbMe_4$ (δ (^{207}Pb) = 0 ppm) by setting the ^{207}Pb peak of $MAPbCl_3$ measured at 293 K to -647.5 ppm.

ToF-SIMS measurement

ToF-SIMS measurements were performed on a ToF-SIMS.5 instrument from ION-ToF GmbH operated in spectral mode using a pulsed 30 KeV Bi^{3+} primary bean with an ion current of 0.48 pA. The analyzed area used was a square of 70 μm × 70 μm, and the depth profile was a square of 210 μm × 210 μm using a 10 keV Ar cluster.

Grazing-incidence wide-angle X-ray scattering measurement

In situ GIWAXS measurements were performed at BL17B1 beamline, Shanghai Synchrotron Radiation Facility (SSRF). The monochromated energy of the X-ray source was 18 keV, and the incidence angle was 0.4°. The correction of the sample-to-detector distance was calibrated with a lanthanum hexaboride (LaB6) sample.

Hyperspectral microscopy measurement

The *in-operando* EL mapping was performed using a wide-field hyperspectral microscopy (IMA VISTM, Photon Etc.) with a 20x air objective. Encapsulated PeLEDs were operated with a Keithley 2450 source meter at a constant bias during the measurement. The camera scanned across 550 nm to 750 nm wavelength window with a step of 2 nm and 1 s camera integration per step.

Transient absorption measurement

The output of a Ti:sapphire amplifier system (Spectra Physics Solstice Ace) operating at 1 kHz and generating ~100-fs pulses was split into the pump and probe beam paths. The 400-nm pump pulses were created by sending the 800-nm fundamental beam of the Solstice Ace through a second harmonic generating (SHG) beta barium borate (BBO) crystal of 1-mm thickness (Eksma Optics). Wavelength tunable pump pulses (e.g., 630-nm pump) were created by sending the 800-nm fundamental beam through a TOPAS optical parametric amplifier (OPA). The pump was blocked by a chopper wheel rotating at 500 Hz while a computer operated a mechanical delay stage (Newport XPS-C8) to adjust the delay between the pump and the probe. The visible broadband beam (520-780 nm) was generated in a home-built noncollinear optical parametric amplifier (NOPA), and the white light was split into two identical beams (probe and reference) by a 50/50 beamsplitter. The reference beam passing through the sample did not interact with the pump, which allows for correcting for any shot-to-shot fluctuations in the probe that would otherwise greatly increase the structured noise in the experiments. Based on this arrangement, small signals with a $\Delta T/T \sim 10^{-5}$ could be measured. The transmitted probe and reference pulses were collected with an InGaAs dual-line array detector (Hamamatsu G11608-512DA, spectrograph: Andor Shamrock SR-303i-B) driven and read out by a custom-built board (Stresing Entwicklungsbüro).

Optical simulation

The emissive characteristics of PeLEDs considering photon recycling were calculated using a recently proposed method based on transfer matrix formalism (TMF)[47,48]. 20 isotropic dipoles were assumed to be evenly distributed over the perovskite layer. Transition dipole moment (TDM) orientations in perovskite films were determined by angle-dependent PL measurements. The parameters used for the fabricated devices are shown in Supplementary Table 3, where the refractive indices for the MM-MOPA perovskite films were obtained using a spectroscopic ellipsometer.

Density functional theory calculation

The calculations were carried out at the density functional theory (DFT) level with Vienna Ab Initio Simulation Package (VASP 6.1.0)[49, 50] using the projector augmented wave method[51, 52]. The exchange-correlation interaction was treated with the generalized gradient approximation (GGA) parameterized by Perdew, Burke and Ernzerhof (PBE)[53]. The DFT-D3[54] method was used to describe long-range van der Waals interactions.

For surface calculations, we cut the $CsPbI_3$ supercell structure along the crystalline plane (001). To avoid the interaction between the repeated images, a vacuum layer of 20 Å was created in the out-of-plane direction of the box. The Brillouin zone integration was sampled with a 2 × 2 × 1 k-points grid with an energy cutoff of 450 eV unless otherwise specified. Ab initio molecular dynamics (AIMD) calculations were performed in the NVT ensemble. In these simulations, two MPPA molecules, two MBA molecules and one MOPA molecule were used in the AX-terminated surface model (consistent with the experimental ratio). Among these, the MOPA exhibits three connection modes: head, tail, and double-end. The control model has an equal number of MPPA and MBA on the surface. The AX-terminated surface calculations use models with both MPPA and MBA on the surface, and the only difference is whether MOPA exists. For the BX-terminated surface model, we cut the BX surface of perovskite and placed one MOPA on this surface, thereafter constructing BX surface models of the MOPA employing three distinct connection configurations. The simulations of the BX surface model were conducted using the similar method.

For density of states (DOS) study, we built the stoichiometric supercells of 320, 480 and 850 atoms, respectively, terminated mostly with the CsI (001) plane, as well as the (100) and (010) planes to model the perovskite with different dimensionalities[55-58]. Brillouin zone was sampled by using a Gamma point and the cutoff energy of plane-wave basis was set to 200 eV. The force was converged to less than 0.01 eV/Å.

Defect density calculation

The hole-only devices with a structure of ITO/PEDOT:PSS/PTAA/PVP/Perovskite/MoO_3/Ag are fabricated. The *I-V* behavior of the devices had three regimes defined by slope k: an Ohmic regime ($k = 1$), a trap-filled limited (TFL) regime ($k > 3$) and a Child regime ($k = 2$). The defect density (n_t) can be determined by the trap-filled limit voltage (V_{TFL}) using the equation (1):

$$n_t = 2\varepsilon_0\varepsilon_r V_{TFL}/eL^2 \quad (1)$$

where ε_0 is the vacuum permittivity, ε_r is the relative dielectric constant, V_{TFL} is the onset voltage of the TFL region, *e* is the electron charge and *L* is the thickness of the perovskite film.

Exciton binding energy calculation

The exciton binding energy was calculated by using the Arrhenius equation (2):

$$I(T) = I_0/(1 + Ae^{-E_b/k_B T}) \quad (2)$$

where I_0 is the integrated PL intensity at 120 K, E_b is the exciton binding energy, and k_B is the Boltzmann constant.

Conductivity calculation

The conductivity (σ) was calculated by using the equation (3):

$$\sigma = l/RA \quad (3)$$

where *l* is the channel length, *R* is the resistance, and *A* is the cross-sectional area.

45 Gunawan, O. et al. Carrier-resolved photo-Hall effect. *Nature* **575**, 151-155 (2019).

46 Lee, S., & Noh, J. H. Steady-state transporting properties of halide perovskite thin films under 1 sun through photo-Hall effect measurement. *J. Phys. Chem. C* **126**, 9559-9566 (2022).

47 Cho, C. et al. The role of photon recycling in perovskite light-emitting diodes. *Nat. Commun.* **11**, 611 (2020).

48 Cho, C. & Greenham, N. C. Computational study of dipole radiation in re-absorbing perovskite semiconductors for optoelectronics. *Adv. Sci.* **8**, 2003559 (2021).

49 Kresse, G. & Joubert, D. From ultrasoft pseudopotentials to the projector augmented-wave method. *Phys. Rev. B* **59**, 1758 (1999).

50 Blöchl, P. E. Projector augmented-wave method. *Phys. Rev. B* **50**, 17953-17979 (1994).

51 Kresse, G. & Hafner, J. Ab initio molecular dynamics for open-shell transition metals. *Phys. Rev. B* **48**, 13115 (1993).

52 Kresse, G. & Furthmüller, J. Efficiency of ab-initio total energy calculations for metals and semiconductors using a plane-wave basis set. *Comput. Mater. Sci.* **6**, 15-50 (1996).

53 Perdew, J. P., Burke, K. & Ernzerhof, M. Generalized gradient approximation made simple. *Phys. Rev. Lett.* **77**, 3865-3868 (1996).

54 Grimme, S., Antony, J., Ehrlich, S. & Krieg, H. A consistent and accurate ab initio parametrization of density functional dispersion correction (DFT-D) for the 94 elements H-Pu. *J. Chem. Phys.* **132**, 154104 (2010).

55 Ravi, V. K. et al. Origin of the substitution mechanism for the binding of organic ligands on the surface of $CsPbBr_3$ perovskite nanocubes. *J. Phys. Chem. Lett.* **8**, 4988-4994 (2017).

56 Dang, Z. et al. In situ transmission electron microscopy study of electron beam-induced transformations in colloidal cesium lead halide perovskite nanocrystals. *Acs Nano* **11**, 2124-2132 (2017).

57 ten Brinck, S. & Infante, I. Surface termination, morphology, and bright photoluminescence of cesium lead halide perovskite nanocrystals. *ACS Energy Lett.* **1**, 1266-1272 (2016).

58 Akkerman, Q. A. et al. Solution synthesis approach to colloidal cesium lead halide perovskite nanoplatelets with monolayer-level thickness control. *J. Am. Chem. Soc.* **138**, 1010-1016 (2016).

Acknowledgments: This work is financially supported by National Key Research and Development Program of China (2022YFE0200200 and 2022YFB3602900). We acknowledge financial support from the National Natural Science Foundation of China (Nos. 62174104, 62321166653 and 51972137), the Program of Shanghai Academic/Technology Research Leader (22XD1421200), the Shanghai Natural Science Foundation (23ZR1423300), the Shuguang Program of Shanghai Education Development Foundation and Shanghai Municipal Education Commission (No. 22SG40), the Innovative Capacity Building Foundation of Jilin Province Development and Reform Commission (2023C034-5), and the Science and Technology Planning Project of Jilin Province (20230101020JC). K.J. acknowledges Royal Society Studentship. S.D.S. thanks Royal Society and Tata Group (UF150033) and funding from European Research Council (HYPERION, No. 756962) and Engineering and Physical Sciences Research Council (EPSRC, EP/R023980/1, EP/V027131/1). We thank the staff from BL17B1, BL02U2, and BL19U2 beamlines of SSRF for providing the beam time and User Experiment Assist System of SSRF for their help and the Supercomputing Center of University of Science and Technology of China for simulations. We thank L. Zhang at Jilin University for providing partial computational resource during the manuscript revision process, G. Xie at Xiamen University for angle-dependent PL measurements and Q. Lin at Wuhan University for optical constant measurements.

Author contributions: X.Y. and N.W. conceived the idea and guided the work. L.K. and Y.W. fabricated and tested the LEDs. Y.S. performed EL kinetics measurements and analyzed the data under N.C.G.'s guidance. K.J. performed hyperspectral imaging measurements with S.D.S.'s guidance. L.D. and S.M. performed TA characterisation and analyzed the data under the guidance of S.D.S. and R.H.F. Y.Y. carried out in situ GIWAXS measurements and directed the data analysis. B.Z., Y.L. and Z.L. carried out theoretical calculations. W.L and C.C. carried out optical simulations. J.D. performed NMR, KPFM, excitation-intensity-dependent PLQYs and temperature-dependent PL measurements. J.F. helped to fabricate perovskite films and collect the data. L.K. wrote the manuscript, which was revised by N.C.G., N.W. and X.Y. All authors discussed the results and commented on the paper.

Data availability: The data that support the findings of this study are available at [url to be added in proof].

Competing interests: The authors declare no competing interests.

Extended Data Fig. 1 | DOS analysis. Electronic DOS curves for $CsPbI_3$ with different atomic numbers. The reduction in perovskite dimensionality is simulated by decreasing the number of atoms. As the dimensionality of $CsPbI_3$ decreases, the antibonding states are pushed to lower energies, and the bonding states just below the Fermi level are, conversely, pushed to higher levels, suggesting a weakened hybridization and bonding.

Extended Data Fig. 2 | Optical characterisation of perovskite thin films. a-d, PL spectra of perovskite thin films with different amounts of MOPA (**a**), MBA (**b**), MPPA (**c**) and mixed MBA and MPPA (**d**) ligands. The Pb concentration is fixed at 0.12 M. **e**, PL spectra of MM-MOPA perovskite films with different amounts of MOPA (the molar concentrations of MOPA are from 0.01 - 0.05 M, with Pb, MBA and MPPA concentrations fixed at 0.12 M, 0.06 M, and 0.06 M, respectively). **f**, Time-resolved PL spectra of perovskite films with MBA, MPPA, and MOPA, respectively.

Extended Data Fig. 3 | XPS, FTIR, and NMR studies. a,**b**, XPS spectra of Pb 4*f* (**a**) and O 1*s* (**b**) for the perovskites without and with MOPA. The Pb 4*f* peaks in MOPA-perovskite were shifted towards lower binding energies, while the O 1*s* peak of methoxy group was shifted to a higher binding energy compared with MOPA. This is caused by the interaction between perovskite and methoxy group of MOPA. **c**, FTIR spectra of the MOPA molecule and MOPA-perovskite. The C-O stretching vibration peaks of the MOPA are shifted to lower wavenumbers when the methoxy group of MOPA interacts with perovskite. **d**, Solid-state ^{207}Pb NMR spectra for the perovskites without and with MOPA. The ^{207}Pb NMR signal of the perovskite centered at 1,560 ppm was shifted to 1,657 ppm upon incorporating MOPA.

Extended Data Fig. 4 | In situ GIWAXS characterisation of perovskite thin films. a,**b**, Integrated one-dimensional GIWAXS spectra (**a**) and zoomed-in region (**b**) of the MM-MOPA perovskite films. The signals are assigned by analysing the diffraction peaks of the corresponding X-ray diffraction patterns (Supplementary Fig. 7).

Extended Data Fig. 5 | Photophysical characterisation of perovskite thin films. a,**b**, Two-dimensional map of temperature-dependent PL spectra of M-MPPA (**a**) and MM-MOPA (**b**) perovskite films. **c**,**d**, The fitted curves of the integrated PL intensity as a function of 1/*T* for M-MPPA (**c**) and MM-MOPA (**d**) perovskite films.

Extended Data Fig. 6 | Stability characterisation of perovskite thin films. a,**b**, Time-dependent PL intensity measurements for the M-MPPA and MM-MOPA perovskite films in ambient air (35% humidity, 25 ºC) for 60 min (**a**) and under 365 nm UV irradiation (**b**).

Extended Data Fig. 7 | Device performance of PeLEDs. Electroluminescence (EL) spectra **a**,**d**, *J-V-L* **b**,**e**, and corresponding EQE-*J* **c**,**f**, curves for the MM-MOPA based PeLEDs emitting at 627 nm (**a-c**) and 645 nm (**d-f**), respectively.

Extended Data Fig. 8 | Operational lifetime of PeLEDs. a,**b**, Half-lifetime (T_{50}) measurements for MM-MOPA based PeLEDs emitting at 627 nm (**a**) and 638 nm (**b**), respectively.

Extended Data Fig. 9 | Nanoscale EL heterogeneity of PeLEDs. a-f, Hyperspectral EL images of M-MPPA (**a**) and MM-MOPA (**d**) based PeLEDs at an operating voltage of 6 V. Hyperspectral EL intensity images of M-MPPA (**b**,**c**) and MM-MOPA (**e**,**f**) based PeLEDs at operating voltages of 6 V (**b**,**e**) and 8V (**c**,**f**). EL signals were collected from 550 to 750 nm. Scale bar, 10 µm.

Extended Data Table 1 | Summary of device performance for recently reported pure-red PeLEDs with high performance.

λ_{EL}, the central wavelength of PeLEDs; EQE_{Max}, maximum external quantum efficiency; T_{50}, the device operating half-lifetime.

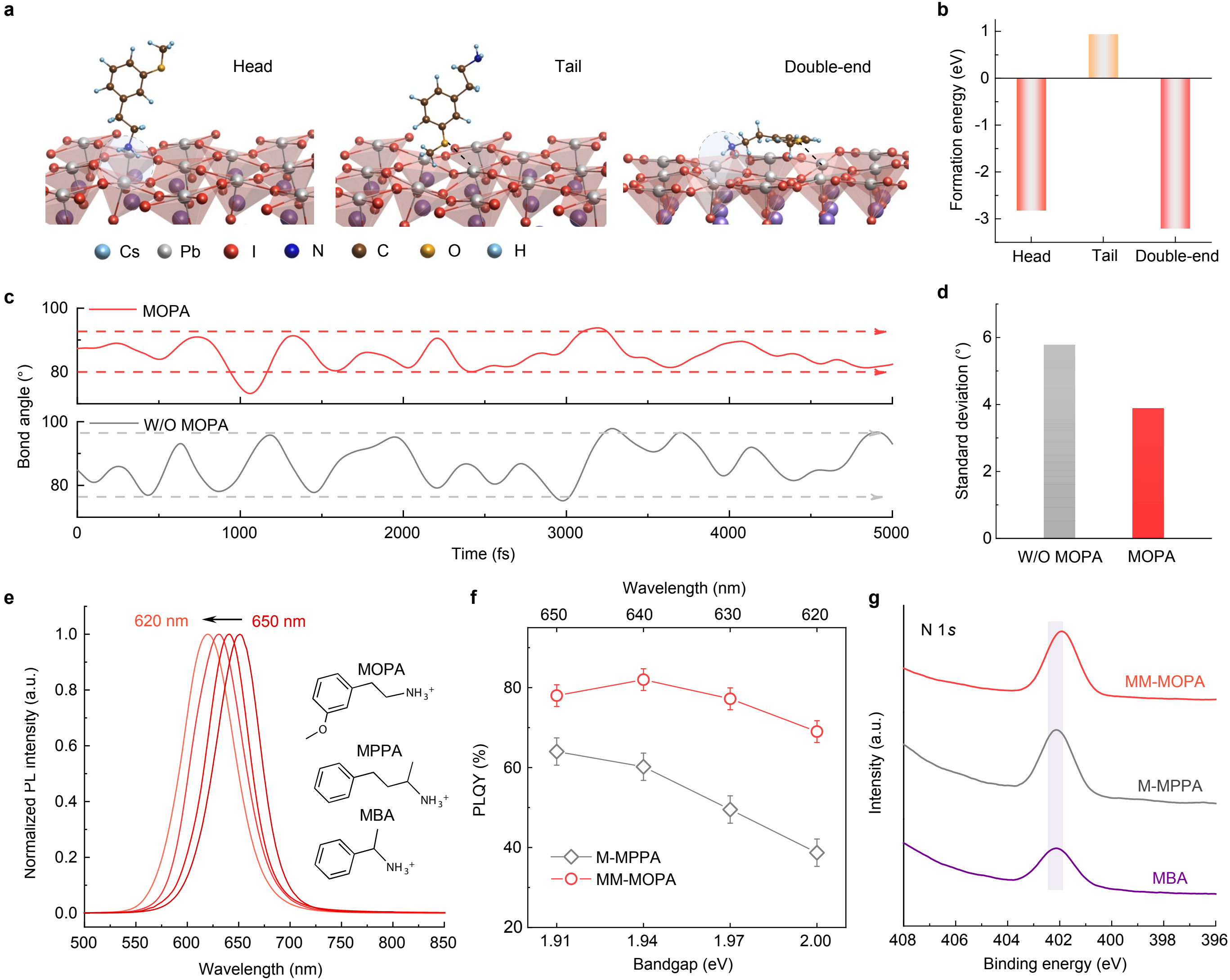
a
Head
Tail
Double-end
Cs
Pb
I
N
C
O
H
b
Formation energy (eV)
1
0
-1
-2
-3
Head
Tail
Double-end
c
MOPA
W/O MOPA
Bond angle (°)
100
80
100
80
0
1000
2000
3000
4000
5000
Time (fs)
d
Standard deviation (°)
0
2
4
6
W/O MOPA
MOPA
e
620 nm
650 nm
Normalized PL intensity (a.u.)
0.0
0.2
0.4
0.6
0.8
1.0
500
550
600
650
700
750
800
850
Wavelength (nm)
MOPA
NH$_3^+$
O
MPPA
NH$_3^+$
MBA
NH$_3^+$
f
Wavelength (nm)
650
640
630
620
PLQY (%)
20
40
60
80
1.91
1.94
1.97
2.00
Bandgap (eV)
M-MPPA
MM-MOPA
g
N 1*s*
Intensity (a.u.)
MM-MOPA
M-MPPA
MBA
408
406
404
402
400
398
396
Binding energy (eV)

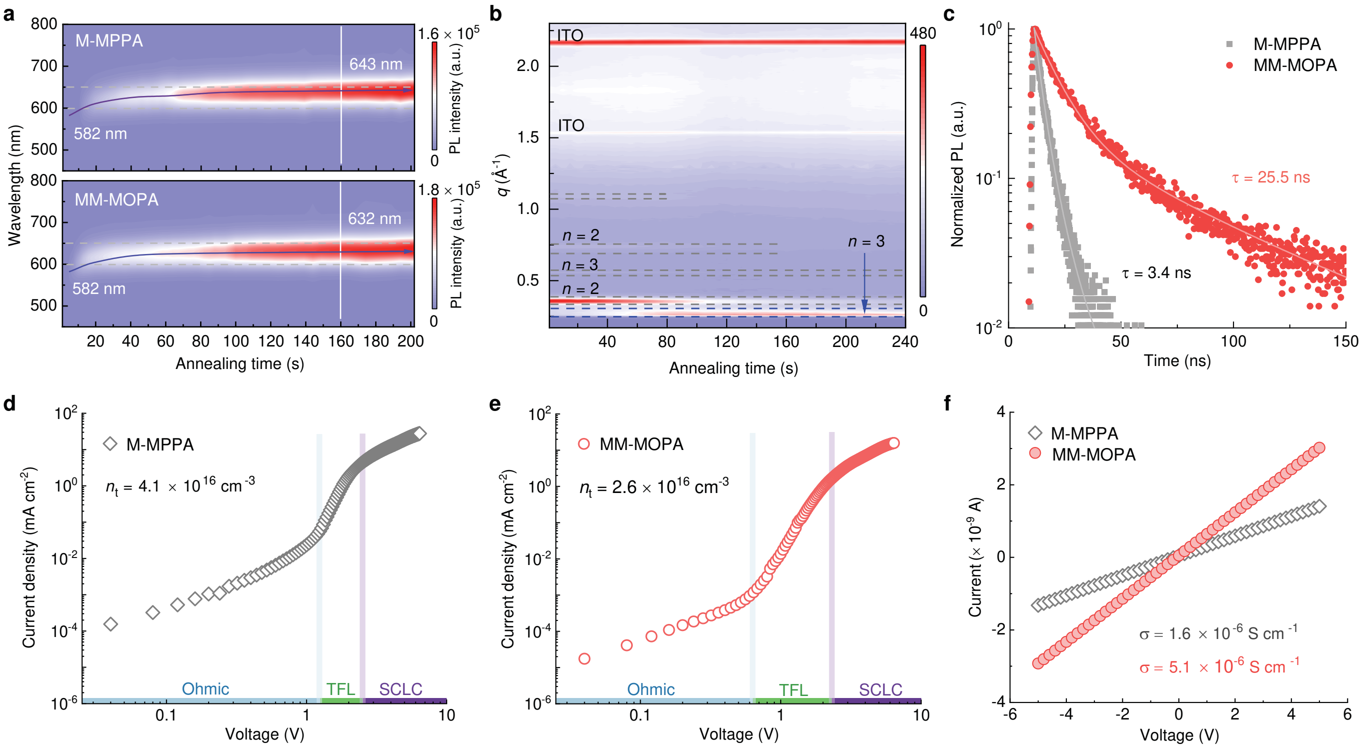
a
M-MPPA
643 nm
582 nm
1.6 × 10^5
PL intensity (a.u.)
0
MM-MOPA
632 nm
582 nm
1.8 × 10^5
PL intensity (a.u.)
0
Wavelength (nm)
800
700
600
500
20 40 60 80 100 120 140 160 180 200
Annealing time (s)
b
ITO
ITO
n = 2
n = 3
n = 2
n = 3
480
0
q (Å^-1)
2.0
1.5
1.0
0.5
40 80 120 160 200 240
Annealing time (s)
c
M-MPPA
MM-MOPA
τ = 25.5 ns
τ = 3.4 ns
Normalized PL (a.u.)
10^0
10^-1
10^-2
0 50 100 150
Time (ns)
d
M-MPPA
n_t = 4.1 × 10^16 cm^-3
Current density (mA cm^-2)
10^2
10^0
10^-2
10^-4
10^-6
Ohmic
TFL
SCLC
0.1 1 10
Voltage (V)
e
MM-MOPA
n_t = 2.6 × 10^16 cm^-3
Current density (mA cm^-2)
10^2
10^0
10^-2
10^-4
10^-6
Ohmic
TFL
SCLC
0.1 1 10
Voltage (V)
f
M-MPPA
MM-MOPA
σ = 1.6 × 10^-6 S cm^-1
σ = 5.1 × 10^-6 S cm^-1
Current (× 10^-9 A)
4
2
0
-2
-4
-6 -4 -2 0 2 4 6
Voltage (V)

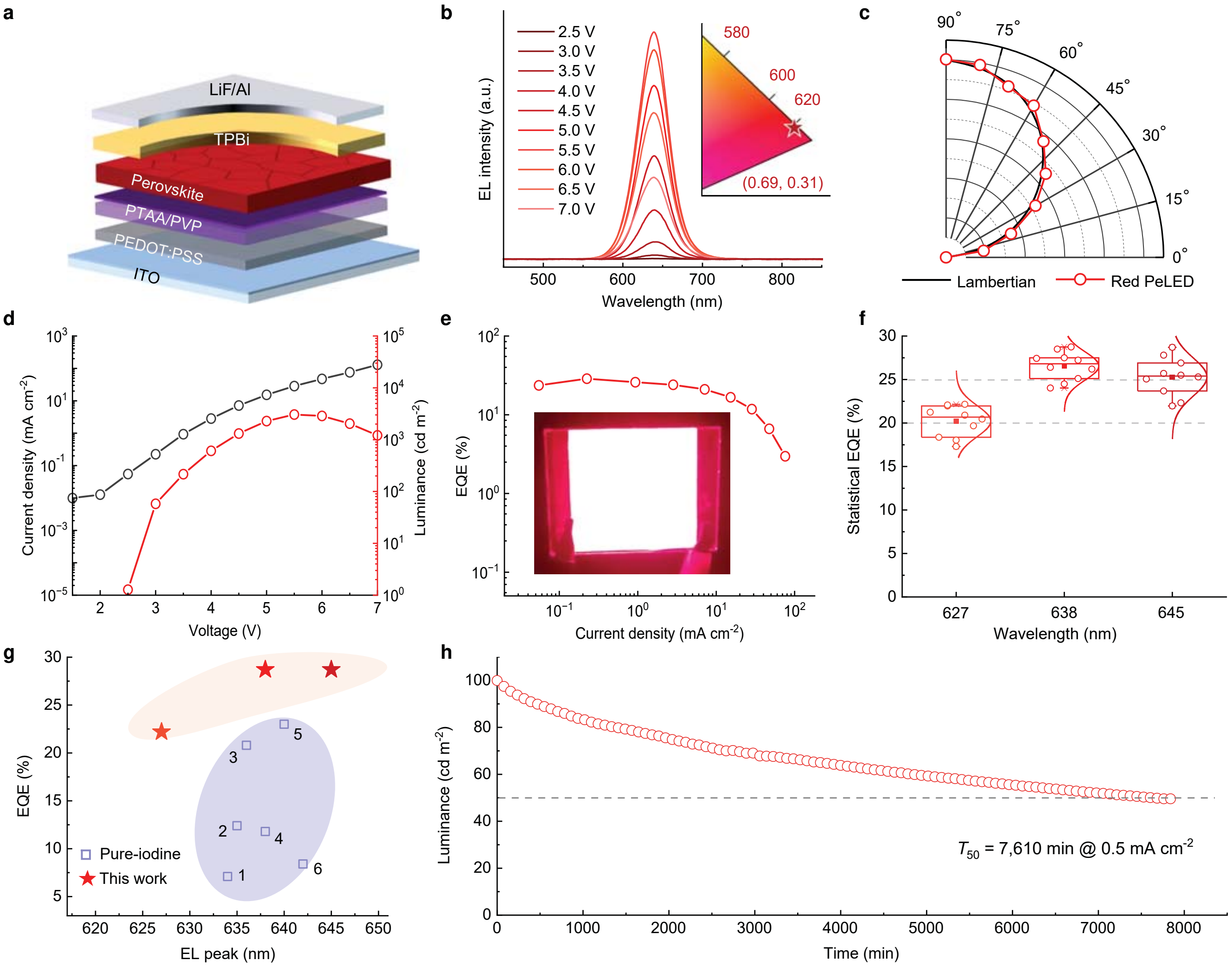
a
LiF/Al
TPBi
Perovskite
PTAA/PVP
PEDOT:PSS
ITO
b
2.5 V
3.0 V
3.5 V
4.0 V
4.5 V
5.0 V
5.5 V
6.0 V
6.5 V
7.0 V
580
600
620
(0.69, 0.31)
EL intensity (a.u.)
500
600
700
800
Wavelength (nm)
c
90°
75°
60°
45°
30°
15°
0°
Lambertian
Red PeLED
d
Current density (mA cm^{-2})
Luminance (cd m^{-2})
10^3
10^1
10^{-1}
10^{-3}
10^{-5}
10^5
10^4
10^3
10^2
10^1
10^0
2
3
4
5
6
7
Voltage (V)
e
EQE (%)
10^2
10^1
10^0
10^{-1}
10^{-1}
10^0
10^1
10^2
Current density (mA cm^{-2})
f
Statistical EQE (%)
30
25
20
15
10
5
0
627
638
645
Wavelength (nm)
g
EQE (%)
30
25
20
15
10
5
1
2
3
4
5
6
Pure-iodine
This work
620
625
630
635
640
645
650
EL peak (nm)
h
Luminance (cd m^{-2})
100
80
60
40
20
0
T_{50} = 7,610 min @ 0.5 mA cm^{-2}
0
1000
2000
3000
4000
5000
6000
7000
8000
Time (min)

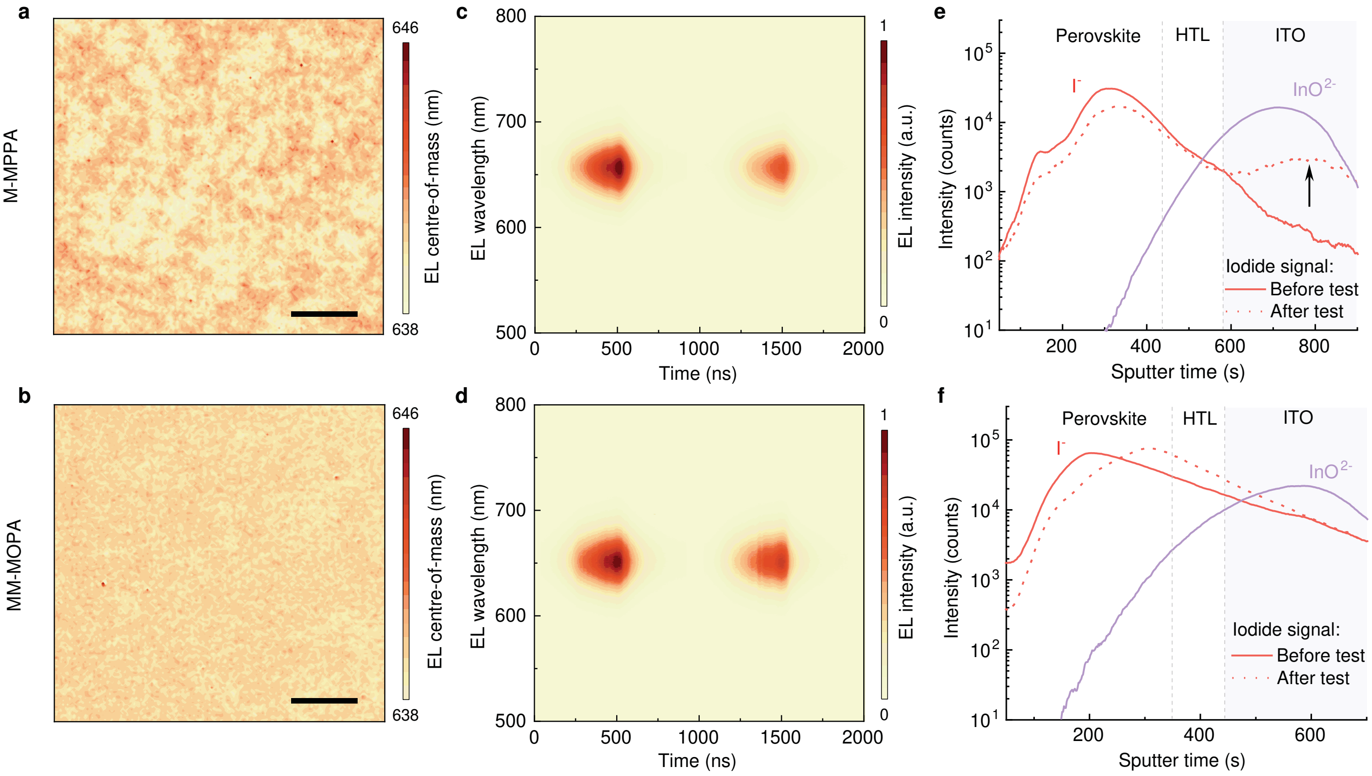
a
M-MPPA
646
638
EL centre-of-mass (nm)
b
MM-MOPA
646
638
EL centre-of-mass (nm)
c
EL wavelength (nm)
800
700
600
500
0
500
1000
1500
2000
Time (ns)
1
0
EL intensity (a.u.)
d
EL wavelength (nm)
800
700
600
500
0
500
1000
1500
2000
Time (ns)
1
0
EL intensity (a.u.)
e
Perovskite
HTL
ITO
I⁻
InO²⁻
Intensity (counts)
10⁵
10⁴
10³
10²
10¹
200
400
600
800
Sputter time (s)
Iodide signal:
Before test
After test
f
Perovskite
HTL
ITO
I⁻
InO²⁻
Intensity (counts)
10⁵
10⁴
10³
10²
10¹
200
400
600
Sputter time (s)
Iodide signal:
Before test
After test